Developing and Evaluating a Risk-Informed Decision Support System for Earthquake Early Warning at a Railway Bridge

Ekin Ozer[a,b]*, Gemma Cremen[c], Pierre Gehl[d], and Enrico Tubaldi[a]

[a]*Department of Civil and Environmental Engineering, University of Strathclyde, Glasgow, UK;* [b]*School of Civil Engineering, University College Dublin, Dublin, Ireland*

[c]*Department of Civil, Environmental and Geomatic Engineering, University College London, London, Ireland*

[d]*Risk and Disaster Prevention Decision, Bureau de Recherches Géologiques et Minières (BRGM), Orléans, France*

* corresponding author: ekin.ozer@ucd.ie

Developing and Evaluating a Risk-Informed Decision Support System for Earthquake Early Warning at a Railway Bridge

Abstract

Earthquake early warning (EEW) systems provide timely information on the arrival of strong seismic waves at a site. Such information can help mitigate the negative impacts of earthquakes on the operation of infrastructure assets. EEW-informed mitigation actions should stem from risk-based decision-making protocols, and EEW benefits should be evaluated for the range of possible rupture scenarios that affect an asset of interest. This paper addresses these challenges specifically for railway bridges by (1) developing a risk-informed EEW decision support system (DSS) for these assets; and (2) quantifying the effectiveness of the proposed EEW-DSS in mitigating seismic risks for railway bridges across relevant rupture scenarios. The proposed EEW-DSS combines information on site-specific seismic hazard, time-dependent EEW algorithm outputs, probabilistic seismic demand modelling, damage/derailment fragilities, and seismic loss models. These modelling components are integrated into a multi-criteria decision-making framework. Value of information theory is then proposed to estimate the loss-mitigation benefits of the EEW-DSS, accounting for varied stakeholder risk priorities as well as dynamic lead-time/accuracy trade-offs related to EEW performance. A multi-span railway bridge is adopted for the case study, which sheds light on the importance of risk-based, uncertainty-informed decision-making to the overall effectiveness of EEW in potentially reducing seismic losses.

Keywords: Earthquake early warning, Decision-support system, Value of information theory, Multi-criteria decision-making, Railway bridges, Train derailment, Seismic risk assessment.

1. Introduction

Earthquake early warning (EEW) systems and algorithms can be used to estimate the size and arrival of earthquake-induced ground motions at a site with seconds to tens of seconds of advance notice. Rapid but important risk-mitigation actions (e.g., automated shut-down procedures or 'Drop, Cover, and Hold on' measures) can then potentially be performed before the shaking hits the area of interest (e.g., Wu & Kanamori, 2008). The idea of using communication technologies for EEW dates to the 1980s and is made possible because digital information travels faster than seismic waves (Heaton, 1985). The physical basis of these systems is that longitudinal primary waves (or P waves) from an earthquake rupture travel faster than the more damaging transverse secondary waves (or S waves). EEW systems can be classified - according to the spatial distribution of the corresponding seismic network used to detect and interpret the incoming earthquake - as regional (e.g., Zuccolo et al., 2020), on-site (e.g., Colombelli et al., 2015), or hybrid (e.g., Iervolino et al., 2006). A recent comprehensive review of the current status of EEW systems and related computational algorithms is provided by Cremen and Galasso (2020).

Decisions for issuing EEW alerts have traditionally been hazard-driven. However, to maximise the practical effectiveness of EEW, there is a need to unify the seismological computations of the system (as well as the related uncertainties) with corresponding risk-based engineering-driven consequence predictions that account for the response of the built environment to earthquakes (e.g., Iervolino et al., 2007). Some work towards this aim has recently been carried out in the literature. For example, Cheng et al. (2014) and Cremen, Velazquez, et al. (2021) investigated the use of engineering-based EEW applications in buildings by translating EEW ground-shaking outputs into building-specific structural responses. Pitilakis et al. (2016) combined EEW seismological information with building-specific fragility functions to investigate the effectiveness of EEW for a hospital. To further facilitate well-informed decision making for EEW, action-specific risk-based consequence predictions should be combined with multi-criteria decision-making (MCDM) frameworks that explicitly account for stakeholder preferences toward the different types of losses that may be incurred (e.g., Le Guenan et al., 2016). This challenge was recently addressed by Cremen and Galasso (2021), who developed an engineering-oriented decision-making methodology for building-specific EEW applications, which has been demonstrated for school buildings (Galasso et al., 2023) and modified for application to a seaport (Cremen et al., 2022).

This study focuses on the effectiveness of EEW for seismic risk management of railway bridges. EEW bridge applications are of interest due to the extensive range of interconnected consequences that can result from the effects

of bridge damage, such as broader transportation and community disruptions. Possible actions that EEW systems can facilitate for a bridge are closing it, restricting its use (e.g., through speed limits/ or lane closures), or keeping it open. However, past studies on EEW have largely overlooked its potential application to seismic risk mitigation for railways. One exception is the study of Sokos et al. (2016),which showed that regional EEW systems could help mitigate seismic risk associated with the Rion-Antirion (Greece) bridge by providing a few seconds of warning (or lead) time that could be leveraged to regulate driving speed and/or prevent bridge crossings during significant earthquake events. Hilbring et al. (2011) focused on derailment-driven decision-making alert thresholds in terms of ground acceleration limits (but did not explicitly consider risk-based consequence predictions). EEW systems have effectively minimised casualties from the Shinkansen train incident during the 2004 Niigata Chuetsu, Japan, earthquake (e.g., Nakamura, 2005; Nakamura et al., 2011). The Bay Area Rapid Transit (BART) system in California has an EEW-triggered automated train-braking mechanism (e.g., Strauss & Allen, 2016).

The accuracy of EEW outputs is a critical consideration in evaluating its effectiveness and has been addressed in many previous studies (e.g., Minson et. al., 2018; Wald 2020; Cremen, Zuccolo, et al., 2021). EEW accuracy is influenced by the different levels of uncertainty associated with the estimated parameters used for making decisions (e.g., real-time location and magnitude estimates and ground-motion intensity at the site of interest). Some of these uncertainties can be reduced as more information is gathered about an incoming event, which comes at the expense of decreased warning time (e.g., Iervolino et al., 2006). Further uncertainties also stem from estimating losses induced by the incoming earthquake and the consequences of actions taken to mitigate risk. Probabilistic frameworks can effectively handle these uncertainties in the decision-making process and their potential influence on false and missed alarms (e.g., Iervolino et al., 2007; Cremen & Galasso, 2021). However, from an analysis of existing literature, it is clear that most investigations of EEW accuracy focus only on single earthquake scenarios (e.g., Minson et al., 2017; Zuccolo et al., 2021). An exception is the study of Minson et al. (2019), which examined various earthquake catalogues in California to illustrate the best-alerting strategy for EEW.

A value of information (VoI) framework (Zonta et al., 2014) can be utilised to investigate EEW effectiveness from a decision support perspective (Wu et al., 2013). The concept of VoI is based on the average value a stakeholder is willing to pay for more information to support their decision making (e.g., Howard, 1966). In this context, it denotes the savings from the loss-mitigation measures triggered by the information from an EEW system. VoI began to play an important part in civil infrastructure decisions with the pioneering works of Pozzi and Der Kiureghian (2011) and Thons and Faber (2013) on the VoI of structural health monitoring. A comprehensive review of VoI-based civil infrastructure decision-making can be found in Zhang et al. (2021). However, to the authors' knowledge, the VoI concept has not yet been applied to quantify benefits of EEW across possible earthquake scenarios that could affect a railway bridge.

To address the identified gaps and ongoing challenges, this paper develops a risk-informed earthquake early warning decision support system (DSS) for the seismic risk management of railway bridges. This work is an extended version of this recent conference paper (Ozer et al. 2023). The DSS is based on the engineering-oriented MCDM methodology introduced in Cremen and Galasso (2021) but innovates by integrating enhanced time-dependent intermediate engineering and loss calculations that account for the seismic behaviour of trains and railway bridges. The VoI concept is then used in a novel procedure for investigating the benefits of the EEW-DSS in terms of earthquake risk mitigation of railway bridges. This involves the development of an effectiveness assessment framework that considers the range of earthquake scenarios affecting a railway bridge and the corresponding reduction in losses that may result due to informed decision making with increasingly accurate earthquake information leveraged in the EEW-DSS (relative to the losses that would occur if the facility would continue to operate as usual). The proposed framework inherently accounts for diversity in stakeholder preferences towards different types of losses (casualties, downtime, and/or monetary costs).

The remainder of the paper is organised as follows. Section 2 illustrates the proposed EEW-DSS for railway bridges; Section 3 introduces the EEW-DSS effectiveness assessment framework; Section 4 demonstrates the methodologies of Sections 2 and 3 for a testbed railway bridge structure in Northeastern Spain, the results of which are presented in Section 5. Finally, Section 6 draws conclusions and proposes potential avenues for future research.

2. Developing a Risk-informed EEW-DSS for Railway Bridges

This section presents the methodological details of the proposed risk-informed EEW-DSS for railway bridges, which involves (1) a performance-based earthquake engineering procedure for estimating real-time seismic losses induced by train derailment; and (2) integration of the outputs of (1) within an MCDM framework that accounts for diverse perspectives on seismic risk. Figure 1 presents a workflow across the components of (1) and (2). Time-varying information used to estimate the magnitude (*M*) and the source-to-site distance (*R)* of the ongoing event via EEW algorithms is collated in the vectors $\boldsymbol{d}$ and $\boldsymbol{s}$, respectively. Ground-motion models (GMMs, or suitable alternatives) are used to predict the probability density function (PDF) $f(\boldsymbol{im}|\boldsymbol{d},\boldsymbol{s})$ of the ground-motion intensity measures (*IM*s) of interest at the considered railway bridge site (collected in a vector, $\boldsymbol{IM}$), based on estimates of *M* and *R* constructed from $\boldsymbol{d}$ and $\boldsymbol{s}$ and following the real-time probabilistic seismic hazard assessment (RTPSHA) approach proposed by Iervolino et al. (2006)**.**

A probabilistic seismic demand model links the *IM*s to the engineering demand parameters (*EDP*s – collected in a vector, $\boldsymbol{EDP}$) of interest via the PDF $f(\boldsymbol{edp}|\boldsymbol{im})$, which are then used to evaluate the occurrence of train derailment, $p(D_{der}|\boldsymbol{im})$. Each *j*-th type of loss consequence associated with train derailment for triggering (*A)* or not ($\bar{A}$) an EEW-induced slow-down of trains at or near the bridge at the time (t_{EEW}) of a triggered alarm - $E(C_j^A|\boldsymbol{d},\boldsymbol{s},t_{EEW})$ - is determined through appropriate damage-to-loss models. These losses - and the importance stakeholders place on reducing them w_j, (i.e., the weight *w* associated with the *j*-th criterion) - are input to an MCDM procedure to determine the optimal real-time EEW-related action to take, A_{opt}. The next subsections describe the various models and variables involved in detail.

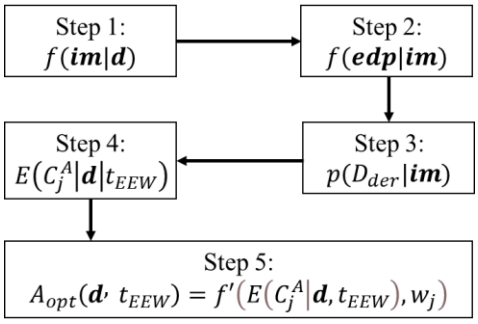

Figure 1. Workflow of the EEW-DSS. Note that $f'(.)$ denotes a generic function.

2.1 Step 1: RTPSHA for EEW, $f(\boldsymbol{im}|\boldsymbol{d})$.

The first step of the methodology is a real-time adaptation of Cornell (1964) probabilistic seismic hazard analysis formulation, following the approach proposed by Iervolino et al. (2006). It estimates the PDF of the site-specific ground-shaking intensities (i.e., $\boldsymbol{IM}$) associated with the incoming event, conditional on the current knowledge of event characteristics from an EEW system, as follows:

$$f(\boldsymbol{im}|\boldsymbol{d},\boldsymbol{s}) = \int_M \int_R f(\boldsymbol{im}|m,r) f(m|\boldsymbol{d}) f(r|\boldsymbol{s}) dm\, dr \quad (1)$$

where $\boldsymbol{d}$ and $\boldsymbol{s}$ are physical measurements or relevant information (e.g., the order in which the seismic stations detect the earthquake) from a seismic network that evolve in time and are respectively leveraged in EEW algorithms to estimate *M* and *R*; $f(m|\boldsymbol{d})$ is the real-time PDF of magnitude conditioned on $\boldsymbol{d}$; $f(r|\boldsymbol{s})$ is the real-time PDF of source-to-site distance conditioned on $\boldsymbol{s}$; and $f(\boldsymbol{im}|m,r)$ can be determined using appropriate GMMs, for instance, in combination with suitable ground-motion correlation models (where appropriate). The exact intensity measures output from this step depend on the probabilistic seismic demand model to be developed (see Section 2.2).

In line with previous work (e.g., Iervolino et al., 2006), it is assumed that $f(m|\boldsymbol{d})$ can be computed according to the following Bayesian approach:

$$f(m|\boldsymbol{d}) = f(m|d_1,d_2,\dots,d_n) = \frac{f(d_1,d_2,\dots,d_n|m) f(m)}{\int_{M_{min}}^{M_{max}} f(d_1,d_2,\dots,d_n|m) f(m) dm} \quad (2)$$

for n magnitude-related real-time measurements (from n seismic sensors, for example), where $f(d_1, d_2, \dots, d_n|m)$ represents the likelihood function (i.e., the joint conditional PDF of $\boldsymbol{d}$) and $f(m)$ is the prior PDF of the magnitude. M_{min} and M_{max} are respectively the minimum and maximum considered magnitudes. The prior distribution of the magnitude, $f(m)$, is assumed to be represented by the Gutenberg-Richter (G-R) relationship in this study:

$$f(m) = \frac{\beta e^{-\beta m}}{e^{-\beta M_{min}} - e^{-\beta M_{max}}} \tag{3}$$

where $\beta = ln(10)b$, b is the slope of the G-R relation, and all other variables are as defined previously. The likelihood component of Equation (4) is computed using the approach adopted by Iervolino et al. (2006). The components of $\boldsymbol{d}$ are assumed to be independent and identically distributed lognormal random variables (Iervolino et al., 2009). Thus,

$$f(d_1, d_2, \dots, d_n|m) = \prod_{k=1}^{n} f(d_k|m) \tag{4}$$

where:

$$f(d_k|m) = \frac{1}{\sqrt{2\pi}\sigma_{ln(d)} d_k} e^{\frac{-1}{2}\left(\frac{ln\, d_k - \bar{\xi}_{ln(d)}}{\sigma_{ln(d)}}\right)^2} \tag{5}$$

The parameters of the lognormal distribution ($\bar{\xi}_{ln(d)}$ and $\sigma_{ln(d)}$) depend on the magnitude-scaling relationship of the associated EEW algorithm adopted (e.g., Allen & Kanamori, 2003) and could also be assumed to depend on k and be adjusted to describe the measurement uncertainty, if relevant. Location uncertainty is herein neglected, given its effects are negligible compared with that of either magnitude or any considered GMM (Iervolino et al., 2009). Therefore, $f(r|\boldsymbol{s})$ reduces to a single (deterministic) value R^*, and Equation (1) simplifies to:

$$f(\boldsymbol{im}|\mathbf{d}) = \int_M f(\boldsymbol{im}|m, R^*) f(m|\boldsymbol{d}) dm \tag{6}$$

2.2 Step 2: Probabilistic Seismic Demand Modelling, $f(\boldsymbol{edp}|\boldsymbol{im})$

This step establishes the relationship between the *IM*s produced in Step 1 ($\boldsymbol{IM}$) and engineering demand parameters (*EDP*s; $\boldsymbol{EDP}$) at the railway bridge. Probabilistic seismic demand models characterising $f(\boldsymbol{edp}|\boldsymbol{im})$ are determined through cloud analysis (e.g., Bazurro et al., 1998), which should account for all sources of uncertainty related to structural modelling, where possible. The *EDP*s included in $\boldsymbol{EDP}$ depend on how derailment is defined (see Section 2.3).

2.3 Step 3: Derailment Analysis, $p(D_{der}|\boldsymbol{im})$.

Train derailment is interpreted in terms of *EDP*s exceeding designated thresholds. Three modes of train derailment on the bridge are considered, in line with Guillaud (2006): i) derailment due to transient vibratory motions of the bridge D_{trans}; and derailment due to permanent deformations on the bridge D_{perm} caused by a damage level *DL,* which refers to either ii) structural damage; or iii) bridge collapse. Fragility curves are developed to quantify the probability of the *der*-th type of derailment for the ground-shaking *IM* outputs from Step 1 (or an adapted version of these), $p(D_{der}|\boldsymbol{im})$, using Monte Carlo sampling to first determine the probability of derailment occurrence as a function of EDPs, $p(D_{der}|\boldsymbol{edp})$, i.e.,

$$p(D_{der}|\boldsymbol{im}) = \int_{\boldsymbol{edp}} p(D_{der}|\boldsymbol{edp})\ f(\boldsymbol{edp}|\boldsymbol{im}) d(\boldsymbol{edp}) \tag{7}$$

2.4 Step 4: Consequence Modelling, $E(C_j^A|\boldsymbol{d}, t_{EEW})$

This component of the methodology computes the real-time expected *j-th* consequence associated with implementing (A) or not ($\bar{A}$) an EEW-triggered slow-down of trains approaching the railway bridge for an incoming earthquake $E(C_j^A|\boldsymbol{d}, t_{EEW})$, leveraging the derailment fragilities developed in Step 3 and time-dependent information on train locations, speed, deceleration ability, and the amount of EEW lead time available. Only derailment-related consequences are considered in this study; consequences associated with structural damage (e.g., repair cost) are

ignored, given that they cannot be reduced through EEW. The examined consequences are expressed in the form of downtime hours (H) and casualties (I).

2.4.1 Quantifying the number of trains at risk of derailment

The consequences associated with either A or $\bar{A}$ depend on the number of trains that may be derailed at the bridge due to the earthquake, which is time-dependent. Let t_{EQ} denote the time the seismic event initiates, t_{EEW} the time that the EEW alarm is issued, t_S the time of arrival of the S wave at the bridge location and t_{SM} the time the strong motion ends, i.e., when 95% of the ground motion's Arias intensity is achieved. The lead time due to earthquake early warning is then $t_{lead} = t_S - t_{EEW}$ (note that only positive t_{lead} values are considered in this study). Two different derailment timeframes are considered: (1) $t_S<t<t_{SM}$ (when D_{trans} is possible); and (2) $t>t_{SM}$ (when D_{perm} is possible). Figure 2 summarises this derailment timeline.

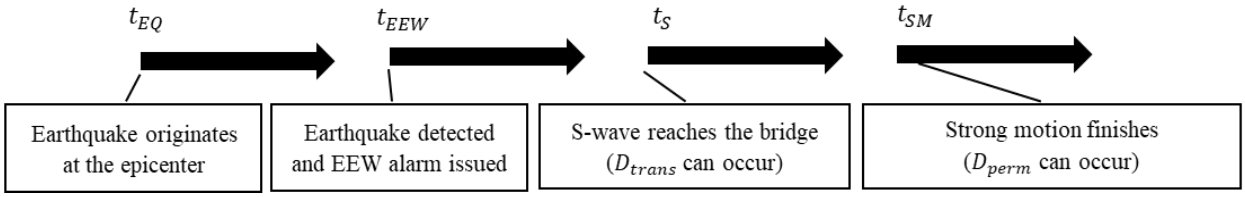

Figure 2. Timeline for earthquake early warning, seismic wave arrival, and the occurrence of derailment.

To identify the potential number of trains that can be derailed, a broad "risk zone" is defined (Figure 3), within which derailment may occur. The risk zone is divided into two separate subzones associated with the two different derailment conditions D_{trans} and D_{perm}. Note that train derailment may also occur outside this zone, but it would be unrelated to the bridge response/damage and is therefore outside the scope of this study. It is assumed that each train travels at speed v_0, and starts decelerating with negative acceleration a at some time (e.g., when an EEW alarm is issued in the case of A), which determines the length of the risk zone. Any trains present within the risk zone at the time of deceleration or the arrival of the s-wave (whichever is sooner) are subject to potential derailment. The longer it takes trains to start decelerating, the longer the risk zone and the higher the number of trains that can potentially derail. This is now described mathematically for both possible actions.

If an EEW-induced slow-down of trains is triggered (A), trains start to decelerate at time t_{EEW}. All trains that cannot decelerate to a stop before entering the bridge are subject to the potential consequences of derailment; therefore, the risk zone extends a length upstream of the bridge equivalent to the theoretical stopping distance ($v_o^2/2a$ m). A train located towards the end of the bridge at t_{EEW} can exit the bridge before the S-wave arrival at t_s (and therefore avoid possible derailment) if there is sufficient lead time. Thus, the end of the risk zone for A is defined by the distance $v_o(t_S - t_{EEW}) - a(t_S - t_{EEW})^2/2$, which is the distance travelled by a train during the lead time afforded by the warning that extends back into the bridge starting from one train length (L_{train}) downstream (see Figure 3). The end of the D_{trans} subzone is defined by the location $v_o(t_{SM} - t_{EEW}) - a(t_{SM} - t_{EEW})^2/2$ upstream of the bridge, which is the distance travelled by a train between the time the EEW is issued and the time the earthquake ends (when D_{perm} becomes possible). Decelerating trains upstream of this distance within $v_o^2/2a$ m of the start of the bridge will enter the bridge at $t>t_{SM}$, and will therefore be subject to potential D_{perm}.

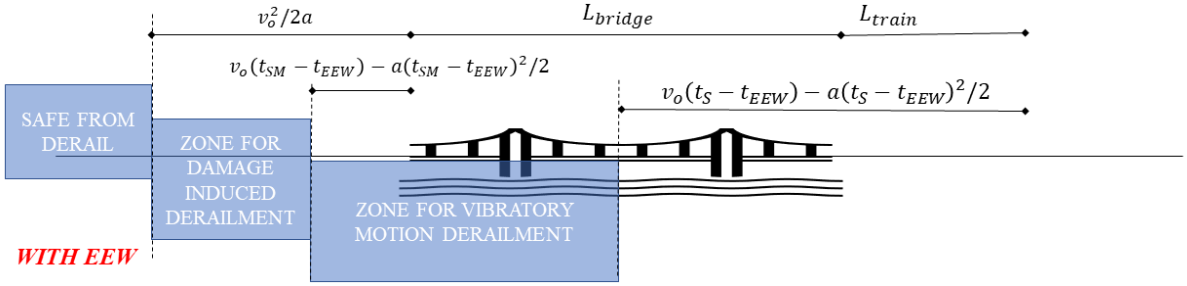

Figure 3. Derailment risk zones and subzones associated with A. Note that L_{bridge} and L_{train} respectively denote the length of the bridge and the length of a train.

For $\bar{A}$, it is assumed that trains will start decelerating at a time $t_W > t_S$. This means that they will travel some distance at the original speed after the s-wave arrives - equal to $v_o(t_W - t_S)$ — that must also be included as part of the risk zone. If the true ground-motion exceeds a high-shaking detection threshold on the train line ($\boldsymbol{IM^* > IM^{upper}}$), t_W is the time at which a corresponding local warning is issued. Otherwise, it is assumed that $t_w = t_{SM}$, resulting in a larger risk zone. As in the case of A, the risk zone extends the stopping distance of a train upstream of the bridge entrance, and the threshold separating both subzones occurs at the upstream distance travelled by a train before t_{SM}. These two distances can respectively be expressed as $v_o(t_W - t_S) + v_o^2/2a$ and $v_o(t_W - t_S) + v_o(t_{SM} - t_W) - a(t_{SM} - t_W)^2/2$. Since trains start to decelerate after (rather than before) t_S, all trains on the bridge at t_W are subject to potential derailment, so the end of the risk zone is simply a train length downstream of the bridge (see Figure 4).

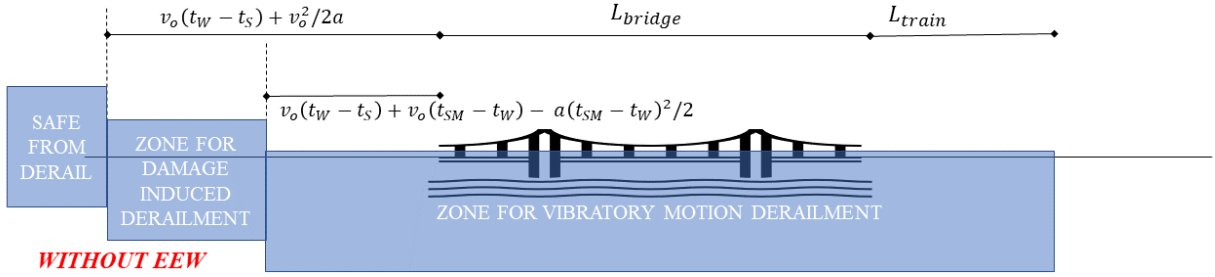

Figure 4. Derailment risk zones and subzones associated with $\bar{A}$. Note that L_{bridge} and L_{train} respectively denote the length of the bridge and the length of a train.

For each case and risk subzone (*sz*), the expected number of trains at risk of derailment can be evaluated as:

$$N_{train}^{A(t_{EEW})}{}_{sz\ der} = \frac{Q}{v_0} L^A(t_{EEW})_{sz\ der} \tag{8}$$

where A and t_{EEW} are replaced with $\bar{A}$ and t_w for no action, Q/v_0 is the average number of trains per unit length, Q is the train flow (i.e., number of trains per given time interval), and $L^A(t_{EEW})_{sz\ der}$ is the action- and time-dependent length of the subzone associated with the *der*-th type of derailment.

2.4.2 Quantifying consequences

Consequences of the *j*-th type (either *H* or *I*) for $\bar{A}$ may then be expressed as:

$$E(C_j^{\bar{A}}|\boldsymbol{d}, t_w) = \int_{\boldsymbol{im}} [E(C_j^{\bar{A}}|\boldsymbol{im}, t_w) f(\boldsymbol{im}|\boldsymbol{d}) + c(t_w)_j^{\boldsymbol{IM_{upper}}}] \, d(\boldsymbol{im}) \tag{9}$$

where $c(t_w)_j^{\boldsymbol{IM_{upper}}}$ is the *j*-th type of consequence associated with exceeding the high-shaking detection threshold (and is 0 otherwise). $c(t_w)_j^{\boldsymbol{IM_{upper}}}$ for H represents an inspection time for each train present within the derailment risk zone of the bridge, and is calculated according to:

$$c(t_w)_1^{\boldsymbol{IM_{upper}}} = h(t_w)^{\boldsymbol{IM_{upper}}} = \sum_{der} N_{train}{}^{\bar{A}(t_w)}{}_{sz\ der}\, h_{insp,train} \tag{10}$$

where $h_{insp,train}$ is the inspection time per train. It is assumed that there are no casualties directly associated with exceeding $\boldsymbol{IM^{upper}}$, i.e., $c(t_w)_2^{\boldsymbol{IM_{upper}}} = i(t_w)^{\boldsymbol{IM_{upper}}} = 0$.

$E(C_j^{\bar{A}}|\boldsymbol{im}, t_w)$ can be divided into separate losses caused by D_{trans} and D_{perm} according to:

$$E(C_j^{\bar{A}}|\boldsymbol{im}, t_w) = E\left(C_j^{\bar{A}}{}_{trans}\middle|\boldsymbol{im}, t_w\right) + E\left(C_j^{\bar{A}}{}_{perm}\middle|\boldsymbol{im}, t_w\right) \tag{11}$$

where, for the *der*-th type of derailment:

$$E\left(C_{j\ der}^{\bar{A}}\middle|\boldsymbol{im},t_w\right) = E(C_{j,train,der})\left(N_{train}{}^{\bar{A}(t_w)}{}_{sz\ der}\right)p(D_{der}) \quad (12)$$

and $E(C_{j,train,der})$ is the expected derailment-induced consequence per train. If $\boldsymbol{im}>\boldsymbol{IM}^{\boldsymbol{upper}}$, $p(D_{der}) = p(D_{der}|M^*,R^*) = \int_{\boldsymbol{edp}} p(D_{der}|\boldsymbol{edp})\ f(\boldsymbol{edp}|M^*,R^*)d(\boldsymbol{edp})$, where $f(\boldsymbol{edp}|M^*,R^*) = \int_{\boldsymbol{im}^*} f(\boldsymbol{edp}|\boldsymbol{im})\ f(\boldsymbol{im}|M^*,R^*)d(\boldsymbol{im}^*)$, M^* is the true magnitude of the incoming event and R^* is as previously defined. In words, this means that the true source parameters of the earthquake are used to calculate the probability of derailment occurrence for cases in which the high ground-shaking detection threshold is estimated to be exceeded. Otherwise, $p(D_{der}) = p(D_{der}|\boldsymbol{im})$, computed from Equation (7). $E(C_{1,train,der}) = E(H_{train,der})$ is the expected time required to rerail a train from the *der*-th type of derailment. $E(C_{2,train,der}) = E(I_{train,der}) = N_p$, where N_p is the number of passengers on each train, such that a train detailment results in casualties to all persons onboard. It is assumed that t_w is exclusively dependent on the source-parameters of the incoming earthquake (represented by $\boldsymbol{d}$ and R^*), and thus $E(C_j^{\bar{A}}|\boldsymbol{d},t_w)$ simplifies to $E(C_j^{\bar{A}}|\boldsymbol{d})$.

Consequences of the *j*-th type (either *H* or *I*) for A are expressed similarly to those for $\bar{A}$ as:

$$E(C_j^A|\boldsymbol{d},t_{EEW}) = \int_{\boldsymbol{im}} E\left(C_j^A\middle|\boldsymbol{im},t_{EEW}\right) f(\boldsymbol{im}|\boldsymbol{d})d(\boldsymbol{im}) + c(t_{EEW})_j^{\boldsymbol{EEW}} \quad (13)$$

where $E\left(C_j^A\middle|\boldsymbol{im},t_{EEW}\right)$ is computed using Equations (11) and (12), substituting A for $\bar{A}$, t_{EEW} for t_w, and $p(D_{der}|\boldsymbol{im})$ for $p(D_{der})$. $c(t_{EEW})_1^{\boldsymbol{EEW}} = h(t_{EEW})^{\boldsymbol{EEW}}$ is the downtime consequence directly associated with triggering the EEW alarm, is calculated analogously to $c(t_w)_1^{\boldsymbol{IM_{upper}}}$. It is assumed that $c(t_{EEW})_2^{\boldsymbol{EEW}} = i(t_{EEW})^{\boldsymbol{EEW}} = 0$.

Equations (9) to (13) reveal inherent trade-offs between A and $\bar{A}$. A typically results in a reduced risk zone compared to $\bar{A}$ (since $t_{EEW} < t_w$, as explained in Section 2.4.1). However, A causes $c(t_{EEW})_j^{\boldsymbol{EEW}}$ losses to occur every time it is issued; the analogous losses for $\bar{A}$, $c(t_w)_j^{\boldsymbol{IM_{upper}}}$, are only incurred if the high-shaking detection threshold is exceeded.

2.5 Step 5: Multi-Criteria Decision-Making, $A_{opt}(\boldsymbol{d},t_{EEW}) = f'\left(E\left(C_j^A|\boldsymbol{d},t_{EEW}\right),w_j\right)$

This component of the methodology accounts for stakeholders' preferences towards the *j-th* type of consequence examined (w_j) as well as the time-dependent expected magnitude of each consequence $E\left(C_j^A|\boldsymbol{d},t_{EEW}\right)$, to determine the real-time optimal decision to take (A_{opt}, i.e., trigger or not a slow-down of trains). The methodology proposed by Cremen and Galasso (2021) is used to determine A_{opt}, leveraging the Technique for Order Preference by Similarity to Ideal Solution method (TOPSIS; Yoon & Hwang, 1995) for decision evaluation.

Stakeholder preferences towards each type of consequence are first used to weight the consequence values determined for A and $\bar{A}$, according to:

$$r_{A,C_j} = \frac{E(C_j^A|\boldsymbol{d},t_{EEW})}{\sqrt{E\left(C_j^{\bar{A}}\middle|\boldsymbol{d}\right)^2 + E(C_j^A|\boldsymbol{d},t_{EEW})^2}} \times w_j \quad (14)$$

where w_j measures the importance of the *j*-th consequence to the decision maker. A and $E(C_j^A|\boldsymbol{d},t_{EEW})$ are appropriately substituted with $\bar{A}$ and $E(C_j^{\bar{A}}|\boldsymbol{d})$ for the case of no action. The optimal action $A_{opt}(\boldsymbol{d},t_{EEW}) \in \{A,\bar{A}\}$ leads to the maximum value of S_i according to:

$$S_i = \frac{y_i^-}{y_i^+ + y_i^-} \quad (15)$$

where $y_i^- = y_1^-$ for A is computed from:

$$y_1^- = \sqrt{\sum_{j=1}^{N_c} \left(v_j^- - r_{A,C_j}\right)^2} \quad (16)$$

v_j^- is the maximum value of $\{r_{A,C_j}, r_{\bar{A},C_j}\}$ and $N_c = 2$ is the total number of considered consequences. y_1^+ is also calculated from Equation (16) by substituting v_j^+ for v_j^-, where v_j^+ represents the minimum value of $\{r_{A,C_j}, r_{\bar{A},C_j}\}$. ($y_2^-$ and y_2^+ are calculated from Equations (14) and (16) by substituting $\bar{A}$ for A).

2.5 Framework for Assessing the Effectiveness of the Developed EEW-DSS System

The concept of VoI is used to quantify the benefits of the developed EEW-DSS in terms of minimising the consequences. Two measures of VoI are used in this study. The first measure $VoI_{1,n_{eq},j}(\boldsymbol{d}, t_{EEW})$ compares, for a given n_{eq} −th earthquake event, the j-th consequences associated with $A_{opt}(\boldsymbol{d}, t_{EEW})$ to those that correspond with EEW information being ignored or unavailable (Wu et al., 2013) where the bridge is operated as usual (action $\bar{A}$). $VoI_{1,n_{eq},j}(\boldsymbol{d}, t_{EEW})$ for a generic earthquake event can therefore be expressed as follows:

$$VoI_{1,n_{eq},j}(\boldsymbol{d}, t_{EEW}) = E(C_j^{\bar{A}}|M^*) - E(C_j^{A_{opt}(\boldsymbol{d},t_{EEW})}|M^*, t_{A_{opt}}) \quad (17)$$

where $t_{A_{opt}} = t_{EEW}$ if $A_{opt}(\boldsymbol{d}, t_{EEW}) = A$ and $t_{A_{opt}} = t_W$ (completely dependent on $\boldsymbol{d}$ and R^*) otherwise. $E(C_j^{\bar{A}}|M^*)$ and $E(C_j^{A_{opt}(\boldsymbol{d},t_{EEW})}|M^*, t_{A_{opt}})$ are respectively computed based on Equations (9) and (13), by substituting M^* for $\boldsymbol{d}$.

A second EEW VoI measure $VoI_{2,n_{eq},j}(\boldsymbol{d}, t_{EEW})$ is introduced, which compares for a given available lead time, the j-th consequence incurred by taking $A_{opt}(\boldsymbol{d}, t_{EEW})$ to the j-th consequence corresponding to $A_{opt}(M^*, t_{EEW})$ that is determined based on perfect knowledge of the magnitude (M^*) and location (R^*) of the n_{eq}-th event being available:

$$VoI_{2,n_{eq},j}(\boldsymbol{d}, t_{EEW}) = E(C_j^{A_{opt}(\boldsymbol{d},t_{EEW})}|M^*, t_{A_{opt}}) - E(C_j^{A_{opt}(M^*,t_{EEW})}|M^*, t_{A_{opt}^*}) \quad (18)$$

where $t_{A_{opt}^*}$ refers to $A_{opt}(M^*, t_{EEW})$ and all other variables are as previously defined. $VoI_{2,n_{eq},j}(\boldsymbol{d}, t_{EEW})$ therefore measures the marginal benefits of an ideal EEW system that produces certain and accurate source-parameter information over an EEW system that is affected by the uncertainty in the estimates of source parameters.

A complete quantification of the EEW benefits should account for the range of earthquake scenarios that could affect the bridge site. To address this requirement, the concept of pre-posterior VoI is introduced, which is the expected value of VoI accounting for multiple possible events i.e., $E\left[VoI_{n_{VOI},j}(\boldsymbol{d}, t_{EEW})\right]$, where $n_{VOI} = 1$ or 2. This is obtained with a plain Monte Carlo sampling approach by generating a set of earthquake events (n_{eq}=1,2,… N_{events}) according to the characteristics of area or fault sources potentially affecting the bridge, and then averaging the values of the $VoI_{n_{VOI},k,j}(\boldsymbol{d}, t_{EEW})$ values obtained for each kth event with t_{lead}>0, considering a set of n seismic-sensor measurements used to compute $\boldsymbol{d}$.

3. Case Study

This section demonstrates the development and evaluation of an EEW-DSS for the testbed railway bridge of Mugo Viaducto del Rio in Northeastern Spain (42° 18’ 51.26” N; 2° 55’ 26.75” E). It is noteworthy that in the absence of comprehensive engineering details as well as validated risk- and EEW-related models for the specific bridge of interest, some (potentially simplified) assumptions are made throughout the case study (with relevant details to follow). Therefore, the results of this demonstration should be treated as hypothetical; further site-specific investigations would be needed to determine their validity for a real-life implementation of the EEW-DSS at the bridge.

3.1 Background Information

3.1.1 Bridge Design Details

The testbed structure is a twelve-span railroad bridge viaduct. Figure 5 presents the bridge location and the seismic stations used in the EEW process. This seismic station network comprises 15 accelerometers, 14 high-fidelity broadband seismometers, and five Internet-of-Things-enabled low-cost seismometers (Raspberry Shake 4Ds). The bridge, which has been in service since 2009, spans a total length (i.e., L_{bridge}) of 690 m, supported by a reinforced concrete prestressed deck and rectangular hollow piers with heights ranging between 8 and 45 m. The design drawings and engineering details are not accessible; therefore, characteristic bridge features are obtained where available (Muga Viaduct, 2018; after Manterola Armisen et al., 2008) and augmented with information from Google Earth imagery. Figure 6 provides a reference image of the testbed structure.

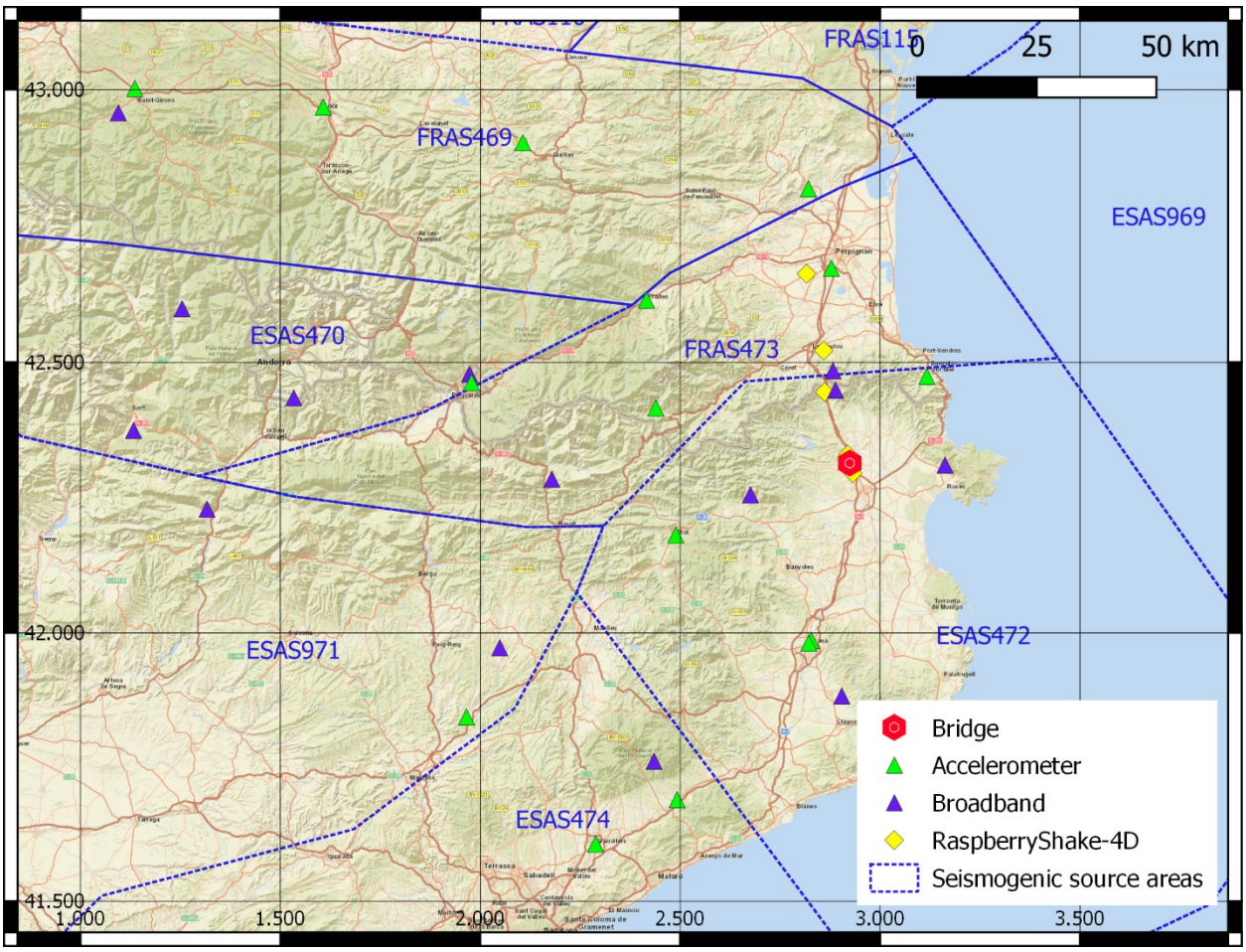

Figure 5. Seismic station network in the testbed region.

Figure 6. Testbed railroad bridge (Image Credit: Google Earth).

Due to the lack of available design details, the pier and deck properties are inferred from those of similar railway bridge viaducts in the area (Martinez-Martin et al., 2013). It is assumed that pier sections are hollow with outer dimensions of 6.8x2.5 m^2 and that longitudinal reinforcement fulfils the 1% minimum design requirement of Eurocode 8. Dead and permanent deck loads are set as 217 kN/m (Martinez-Martin et al., 2013). This corresponds to an approximate 25000 kN axial load at the base of the tallest piers and 250000 kNm and 80000 kNm yield moments in the strong and weak axes, respectively. Figure 7 provides sketches that include the estimated bridge dimensions and pier details used for developing the nonlinear finite element model (see Section 3.1.2).

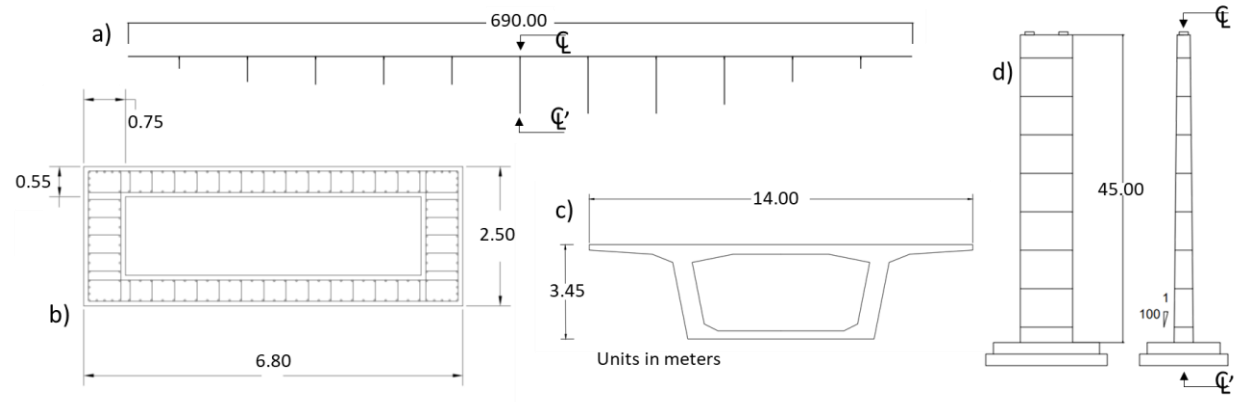

Figure 7. Bridge a) elevation layout; b) deck reinforcement; c) pier cross-section; and d) example pier side views (the pier at the centreline).

3.1.2 Structural Model Details

A 3D finite element model of the bridge is constructed in the OpenSees platform (McKenna, 2011) based on the details of Figure 8, using beam elements and nonlinear fibre sections (at the base). Deck-pier connectivity is assumed to slide in the horizontal direction and transfer deck forces to the piers in the vertical and lateral directions. Deck elements are discretised into five segments of a typical 60-m span length, intersecting with pier pot bearings through fictitious beams. One abutment restrains movement in the longitudinal, vertical, transverse, and torsional directions, and the second abutment is free to move in all directions except the transverse and vertical ones. A "*beamWithHinges*" element is used to model nonlinearity in the pier base element. Figure 8a presents a three-dimensional view of the OpenSees model obtained with OpenSeesNavigator. Figures 8b and 8c display the first (1.03 s) and second (0.91 s) vibration modes in the transverse direction.

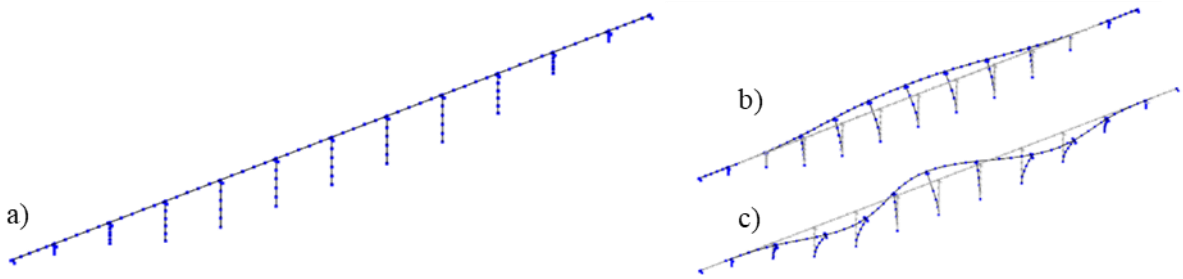

Figure 8. a) Bridge model developed in the OpenSees platform; (b) first (period at 1.03 s); and (c) second (period at 0.91 s) vibration modes in the transverse direction.

3.1.3 Earthquake Scenario Details

Stochastic earthquake scenarios affecting the bridge are generated by sampling events from the seismogenic sources surrounding the site. The G-R distribution parameters of these sources are obtained from the Seismic Hazard Harmonization in Europe (SHARE) project's area source model (Giardini et al., 2013; Woessner et al., 2015; see Table 1). A minimum magnitude cut-off of 4.5 is chosen to prevent the sampling of non-damaging events. Note that *a'* denotes the productivity parameter of the G-R distribution, and all other variables are as defined in Section 2.2.

Table 1. Activity parameters for the selected seismogenic source areas (*ss*).

Area ID	$M_{min,ss}$	$M_{max,ss}$	a'_{ss}	b_{ss}
FRAS469	4.5	6.8	3.2500	1.00
ESAS470	4.5	6.8	3.0000	1.00
ESAS472	4.5	6.8	2.5845	1.03
FRAS473	4.5	6.8	3.0000	1.00
ESAS474	4.5	6.5	3.2000	1.00
ESAS971	4.5	6.8	1.3968	1.03
FRAS115	4.5	6.5	2.1000	1.00
ESAS969	4.5	6.5	3.2707	1.00

For sampling purposes, the weight of a seismogenic source *ss* (γ_{ss}) is quantified as follows:

$$\gamma_{ss} = e^{\alpha_{ss}} \frac{e^{-\beta_{ss} M min_{ss}} - e^{-\beta_{ss} M max_{ss}}}{1 - e^{-\beta_{ss} M max_{ss}}} \tag{19}$$

where $\alpha_{ss} = ln(10)\, a'_{ss}$ and all other variables are as defined previously. Once a given source is sampled using the normalised values of γ_{ss}, the event magnitude is obtained from the G-R distribution, and the event location is randomly generated within the spatial bounds of interest (i.e., assuming that earthquake events are uniformly distributed across the seismogenic source area). Finally, a maximum distance cut-off of 100 km (between the epicentre location and the bridge) is adopted to avoid sampling remote events, likely resulting in negligible damage and consequences. The total number of simulated events is 1000. Removing earthquakes that do not result in positive lead-time for any value of *n* (see Section 3.5 for more details) results in an expected final catalog of $N_{events} = 634$.

3.2 Step 1: RTPSHA

The Allen and Kanamori (2003) EEW magnitude-scaling relationship is adopted in this study, and we neglect any deviations due to station-specific measurement uncertainty. This implies that $\boldsymbol{d} = [\, \tau_1, \tau_2, \ldots \tau_k, \ldots, \tau_n]$, where τ_k denotes the four-second predominant period evaluated from seismic-sensor measurements of the incoming P waves at station *k*. The parameters of the lognormal distribution in Equation (5) are then derived as follows:

$$\bar{\xi}_{ln(\tau)} = \frac{m - 5.9}{7\, log(e)} \tag{20}$$

and

$$\sigma_{ln\,\tau} = \frac{0.16}{log(e)} \tag{21}$$

In this case, the real-time magnitude distribution of Equation (2) for an earthquake from seismic source *ss* may be succinctly expressed as (Iervolino et al., 2009):

$$f(m|\boldsymbol{d}) = \frac{e^{\left(2\mu_{ln\,\tau}\left(\sum_{k=1}^{n} ln\,\tau_k\right) - n\bar{\xi}^2_{ln\,\tau}\right)/2\sigma^2_{ln\,\tau}} e^{-\beta_{ss} m}}{\int_{M_{min}}^{M_{max}} e^{\left(2\mu_{ln\,\tau}\left(\sum_{k=1}^{n} ln\,\tau_k\right) - n\bar{\xi}^2_{ln\,\tau}\right)/2\sigma^2_{ln\,\tau}} e^{-\beta_{ss} m} dm} \tag{22}$$

For each considered earthquake, we simulate information available from an EEW system as follows. τ_k values are first generated at the 34 seismic stations surrounding the site, considering the magnitude of the given event and using Equation (5). These values are then used to compute $f(m|\boldsymbol{d})$ according to Equation (22). In this case, the intensity measure of interest is the spectral acceleration at the fundamental period of the bridge, i.e., $\boldsymbol{IM} = IM = Sa(1.03)$. $f(Sa(1.03)|m, R^*)$ is determined from the epicentral version of the Akkar et al. (2014) GMM for European seismicity, assuming the most common style of faulting in the region (i.e., thrust) and the time-averaged shear-wave velocity to a depth of 30 meters (Vs30) value for the bridge site from the database of Wald and Allen (2007). 500 event-dependent ground-shaking intensity values are finally sampled according to Equation (6). The "true" ground-motion intensity distribution for each earthquake $f(Sa(1.03)|M^*, R^*)$ is determined from the same GMM; 500 samples are also used in this case.

3.3 Step 2: Probabilistic Seismic Demand Modelling

To develop the probabilistic seismic demand model, 221 ground motion records are used as input excitations in the two orthogonal directions for nonlinear time history analyses (NLTHAs). Detailed features of this ground motion dataset can be found in Tubaldi et al. (2021). Uncertainties related to structural modelling are neglected in the absence of relevant data. Bilinear excitation is imposed on the nonlinear finite element model with a Rayleigh damping ratio of 5%. The following set of ***EDP*** is obtained from the NLTHAs: (1) peak pier acceleration (a) responses, both absolute (*abs*) and relative (*rel*) to the ground in the longitudinal (x) and traverse (y) directions, $a_{abs,\,x\,max}$, $a_{abs,\,y\,max}$, $a_{rel,\,x\,max}$, $a_{rel,\,y\,max}$; and (2) peak pier displacement (δ) responses $\delta_{abs,\,x\,max}$ $\delta_{abs,\,y\,max}$ $\delta_{rel,\,x\,max}$ $\delta_{rel,\,y\,max}$. The relationship between each *EDP* and the *IM* is characterised by:

$$EDP = g \cdot IM'^{\lambda} \tag{23}$$

$IM' = Sd_{geom}$, the geometric mean of spectral displacement at the bridge's fundamental period, obtained from $\frac{Sa(1.03)}{\omega^2}$; where ω is the circular frequency). g and λ are constant parameters that define the appropriate probabilistic seismic demand model $f(edp|Sd_{geom})$, based on least squares optimisation in the logarithmic domain. Figure 9 provides the probabilistic seismic demand models for some of the *EDP*s ($a_{abs,\,y,\,max}$, $\delta_{abs,\,y,\,max}$ *and* $\delta_{rel,\,y,\,max}$).

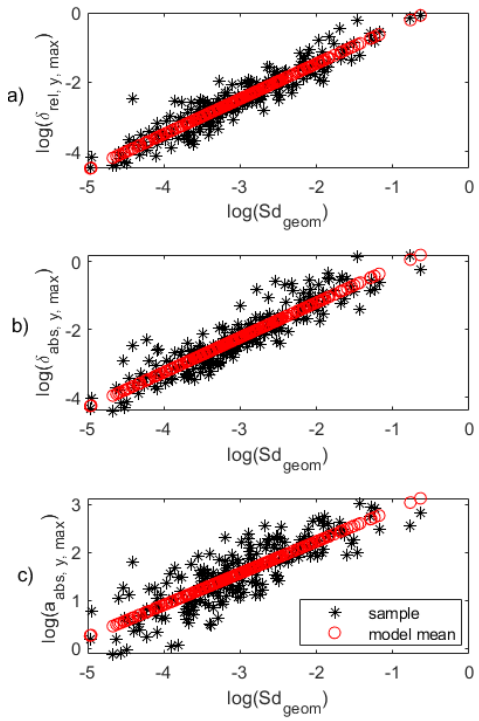

Figure 9. Probabilistic seismic demand model $f(edp|Sd_{geom})$ for a) peak pier displacement relative to the ground; b) peak absolute pier displacement, and c) peak absolute acceleration, all in the transverse direction.

3.4 Step 3: Derailment Analysis

D_{trans} is controlled by $a_{abs,\,y\,max}$ and $\delta_{abs,\,y\,max}$, based on research by the East Japan Railway Company (Shimamura & Yamamura, 2006). $p(D_{trans}|\boldsymbol{edp})$ can then be calculated as follows:

$$\mathrm{p}(D_{trans}|\boldsymbol{edp}) = \begin{cases} 1 \; if \; a_{abs\;y\;max} \geq \overline{a_{abs\;y\;max}} \cap \delta_{abs\;y\;max} \geq \overline{\delta_{abs\;y\;max}} \\ 0 \text{ otherwise} \end{cases} \tag{24}$$

where $\overline{a_{abs\;y\;max}}$ and $\overline{\delta_{abs\;y\;max}}$ respectively denote corresponding acceleration and displacement thresholds, which are equal to 0.3g and 0.07m, according to Guillaud (2006).

This study employs a numerical approach to evaluate bridge global damage (*DL*), assuming it is controlled by the maximum transient deflections of the piers, i.e., *DL* is controlled by $\delta_{rel,\,x\,max}$ and $\delta_{rel,\,y\,max}$ (e.g., Attarchian et al., 2018). In particular, the following conditions are considered to define various *DL*, from 0 (no damage) to 3 (global collapse):

$$DL = \begin{cases} 0 \;\; if \; \frac{\delta_{rel,y\,max}}{\delta_{yield\,y}} + 0.5\,\frac{\delta_{rel,\;x\,max}}{\delta_{yield\,x}} \leq 1 \\ 1 \; if \; \frac{\delta_{rel,\;y\,max}}{\delta_{moderate\,y}} + 0.5\,\frac{\delta_{rel,\;x\,max}}{\delta_{moderate\,x}} \leq 1 \cap \frac{\delta_{rel,\;y\,max}}{\delta_{yield\,y}} + 0.5\,\frac{\delta_{rel,\;x\,max}}{\delta_{yield\,x}} > 1 \\ 2 \; if \; \frac{\delta_{rel,\;y\,max}}{\delta_{collapse\,y}} + 0.5\,\frac{\delta_{rel,\;x\,max}}{\delta_{collapse\,x}} \leq 1 \cap \frac{\delta_{rel,\;y\,max}}{\delta_{moderate\,y}} + 0.5\,\frac{\delta_{rel,x\,max}}{\delta_{moderate\,x}} > 1 \\ 3 \; if \; \frac{\delta_{rel,\;y\,max}}{\delta_{collapse\,y}} + 0.5\,\frac{\delta_{rel,\;x\,max}}{\delta_{collapse\,x}} > 1 \end{cases} \tag{25}$$

where the structure-specific values of $\delta_{yield}, \delta_{moderate}, \delta_{collapse}$, respectively denote the yield, moderate, and collapse displacement limit states and are based on the capacity curves of the pier along *x* and *y*, which are developed for a representative pier at the midspan per Attarchian et al. (2018) (see Figure 10). Note that the collapse capacity is based on the displacement corresponding to 80% of the maximum strength. Damage states are respectively described as i) initial cracks on columns indicating a transition to inelastic behaviour (*DL* =1); ii) post-cracking/spalling and loss of

column anchorage (DL=2); and iii) complete column failure (DL=3) (e.g., Banerjee et al., 2008). Note that DL could also be defined in terms of curvature or drift (Muntasir Billah et al., 2015) or damage index (Karim et al., 2001).

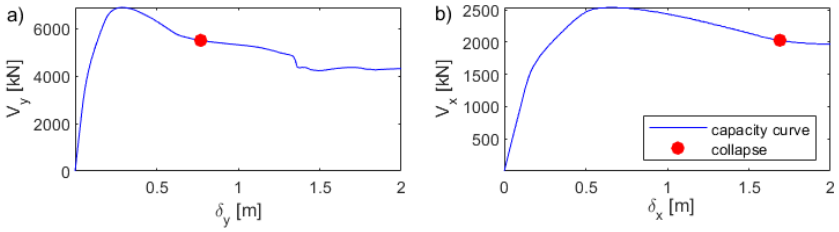

Figure 10. Capacity curves along the a) transverse; and b) longitudinal directions. V denotes shear force and all other variables are as previously defined.

The probability of derailment occurrence due to permanent bridge damage, D_{perm}, can then be evaluated as follows:

$$p(D_{perm}|\boldsymbol{edp}) = \begin{cases} 1 \; if \; DL = 3 \\ \vdots \\ dam_i \; if \; DL = i \; (0 < i < 3 \; \& \; 0 < dam_i < 1) \\ \vdots \\ 0 \; if \; DL = 0 \end{cases} \quad (26)$$

where $dam_1 = 0.25$ and $dam_2 = 0.5$, based on engineering judgement in the absence of appropriate data.

D_{perm} governs over D_{trans}, such that the final value of $\mathrm{p}(D_{trans}|\boldsymbol{edp})$ is computed from:

$$\mathrm{p}(D_{trans}|\boldsymbol{edp}) = \mathrm{p}(D_{trans^m}|\boldsymbol{edp}) - [\mathrm{p}(D_{trans^m}|\boldsymbol{edp}) \cap \mathrm{p}(D_{perm}|\boldsymbol{edp})] \quad (27)$$

where $\mathrm{p}(D_{trans^m}|\boldsymbol{edp})$ is determined from Equation (24).

The derailment fragility curves, expressed in terms of Sd_{geom}, are displayed in Figure 11, along with the collapse fragility curve, $\mathrm{p}(DL = 3|\, Sd_{geom})$.

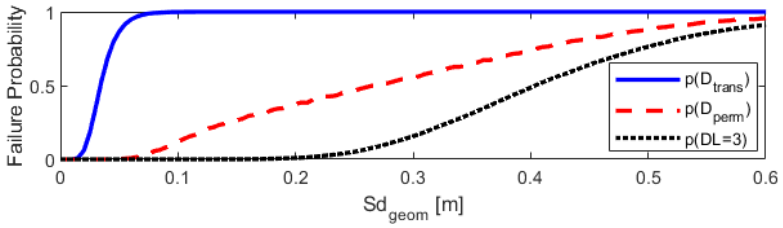

Figure 11. Derailment fragilities and bridge collapse fragility.

3.5 Step 4: Consequence Modelling

In the absence of appropriate available data, the inspection time per train $h_{insp,train}$ is assumed to be one hour, and $\boldsymbol{IM^{upper}} = IM^{upper}$ is taken as $Sa(1.03)$= 0.05 m/s^2. $E(H_{train,trans})$ and $E(H_{train,perm})$ are respectively set as five and 48 hours, using engineering judgment based on similarly observed derailment phenomena (e.g., Ebrahimi et al., 2021). Trains are assumed to be travelling with full passenger capacity, i.e., N_p is 508 people, equivalent to the capacity of a Train à Grande Vitesse (TGV) Duplex (2022) train that uses the bridge. Twelve trains per day pass the bridge, based on relevant example timetables from Red Nacional de los Ferrocarriles Españoles (RENFE) – Société Nationale des Chemins de fer Français (SNCF) (2021), such that Q =0.5 trains/h.

In addition to the parameters above, a is assumed to be -3 m/s^2, v_0 is set equal to 83m/s, $t_{lead} = t_S - t_{EEW} = t_s - t_p - \varepsilon$ (where t_p and ε respectively indicate the time of the p-wave arrival at the n-th station and a trigger delay of 4 seconds, respectively) is computed assuming uniform respective P- and S-wave velocities of v_p= 3.55 m/s and v_s= 6.1 m/s per the CRUST 1.0 model (Laske et al., 2013) and an earthquake depth of 10km (i.e., the most common depth across most of the considered seismogenic sources according to the SHARE area source model). Further assumptions are that $t_{SM} = t_s + 10$ (since 10 seconds corresponds to the median time at which 95% of the Arias intensity is achieved across the ground-motion dataset used), $t_w = t_s + 5$ (when $IM^* > IM^{upper}$), and L_{train}= 200m.

3.5.1 Consequence Modelling Results

Some example consequence modelling results are now examined. Figure 12 presents two of the simulated earthquake scenarios, associated with relatively low (Scenario 149, $M^* = 4.7, R^* = 82\ km$, $E[Sd_{geom}|M^*, R^*] =$ 0.3mm) and high (Scenario 746, $M^* = 6.7, R^* = 57\ km$, $E[Sd_{geom}|M^*, R^*]$=20.7mm) IM values at the bridge, for different numbers of stations n in the seismic network used to compute $\boldsymbol{d}$ in Equations (1) to (6). It can be observed that the empirical cumulative distribution functions $F(Sd_{geom}\,|\boldsymbol{d})$ estimated from 500 Sd_{geom} samples for different values of n are similar for the low-intensity scenario (Scenario 149). This may be explained by the similar nature of the underlying magnitude distributions, which are lower-bounded close to M^*; even for low values of n, the Guternberg-Richter prior components that dominate the distributions ensure that the expected magnitudes are close to M^*. $F(Sd_{geom}\,|\boldsymbol{d})$ distributions differ significantly in the case of the high-intensity scenario (Scenario 746) for $n \leq$ 16 (approximately), where the Guternberg-Richter prior components of the underlying magnitude distributions produce expected magnitudes much smaller than M^*.

Figure 13 visualises – for different values of n used to compute $\boldsymbol{d}$ and the same scenarios depicted in Figure 12 – the expected consequences associated with both issuing and not issuing the alarm, i.e, $E(H^A|\boldsymbol{d}, t_{EEW})$, $E(I^A|\boldsymbol{d}, t_{EEW})$, $E(H^{\bar{A}}|\boldsymbol{d})$, and $E(I^{\bar{A}}|\boldsymbol{d})$ respectively. Also shown are $E(H^A|M^*, t_{EEW})$, $E(I^A|M^*, t_{EEW})$, $E(H^{\bar{A}}|M^*)$, and $E(I^{\bar{A}}|M^*)$, i.e., the expected consequences for both outcomes given perfect knowledge of the source parameters. For the low-intensity earthquake scenario (149), and most examined values of n (in the case of $\boldsymbol{d}$) or all examined values of n (for perfect source-parameter knowledge), A induces inspection downtime losses that are not present for $\bar{A}$, and provides no benefit in terms of casualty reduction.

For the high-intensity earthquake scenario (746), it can be observed that A reduces casualty consequences relative to $\bar{A}$ in (almost) all examined cases. However, the increase or decrease in downtime predicted for A relative to $\bar{A}$ depends on t_{EEW}, which determines the length of the risk zone and underlying subzones, as described in Section 2.4, and increases with increasing n. Increasing t_{EEW} expands the risk zone and the consequences associated with A. This means that it is only beneficial (from a downtime mitigation perspective) to issue the alarm for relatively low t_{EEW} (i.e., low numbers of n), even if there is high uncertainty in the source parameters. The consequence estimates for $\boldsymbol{d}$ generally tend to approach those estimated for M^* as the value of n increases and the accuracy of $f(m|\boldsymbol{d})$ typically improves.

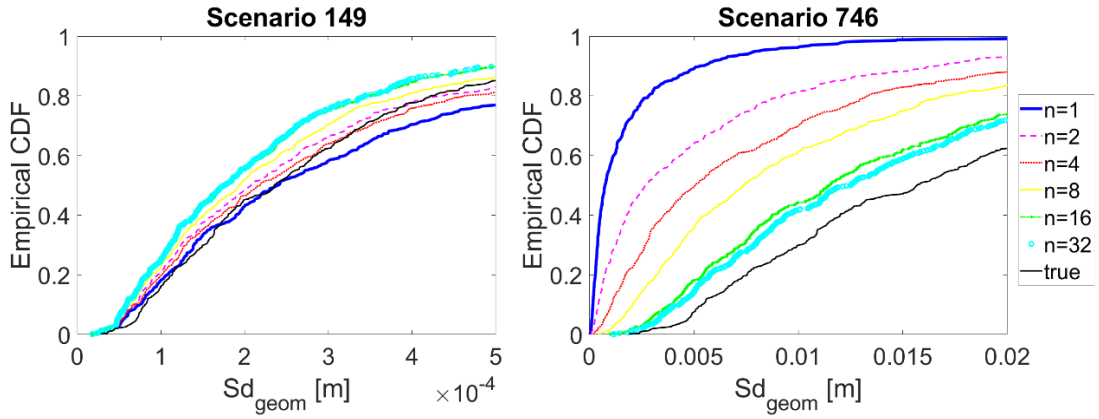

Figure 12. $F\left(Sd_{geom}\,|\boldsymbol{d}\right)$ for (a) a low-intensity (Scenario 149); and (b) a high-intensity (Scenario 746) scenario. Legends indicate the number of triggered stations n from which information is used to compute the distributions; also shown are the true distributions, i.e., $F\left(Sd_{geom}\,|M^*, R^*\right)$

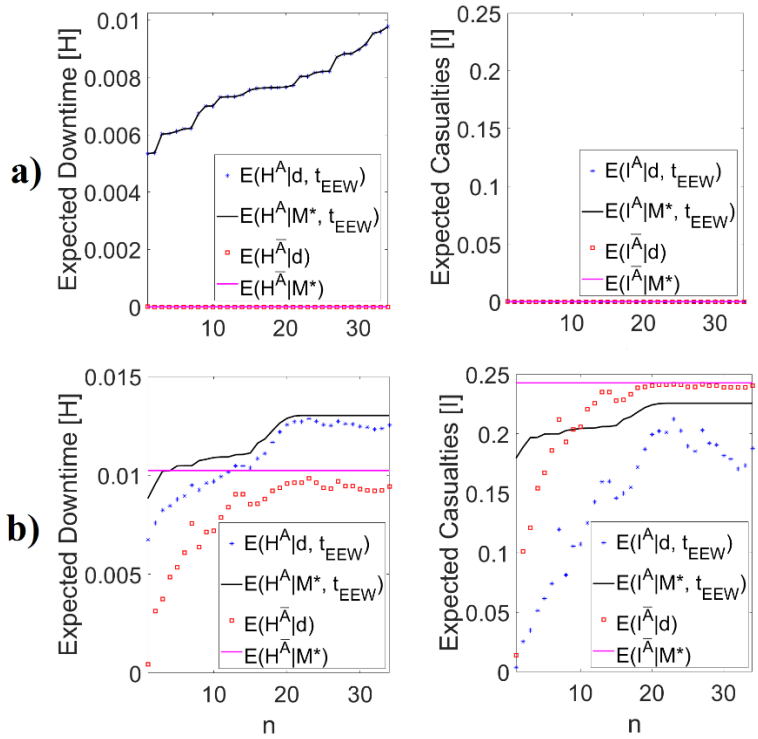

Figure 13. Downtime (H) and casualty (I) consequences associated with (a) a low-intensity (Scenario 149); and (b) a high-intensity (Scenario 746) scenario for a given number of triggered stations, n.

3.6 Step 5: Multi-Criteria Decision Making

This subsection investigates the effects of different w_j on $A_{opt}(\boldsymbol{d}, t_{EEW})$ and $A_{opt}(M^*, t_{EEW})$. Table 2 presents the w_j values considered in these analyses, which are selected to investigate an incremental transition from a casualty-dominant (Case 1) to a downtime-dominant (Case 7) set of stakeholder preferences.

Table 2. Various cases of w_j sets examined in this study.

Consequence/Case	1	2	3	4	5	6	7
Downtime	0.	0.05	0.333	0.5	0.667	0.95	1.0
Casualty	1.0	0.95	0.667	0.5	0.333	0.05	0.

Figure 14 demonstrates how $A_{opt}(\boldsymbol{d}, t_{EEW})$ and $A_{opt}(M^*, t_{EEW})$ are influenced by the different sets of w_j examined, for $n = 1$ and $n = 34$ (and the associated t_{EEW}) and all corresponding earthquake scenarios considered. The results are expressed in terms of $E[Sd_{geom}|M^*, R^*]$ values obtained for each earthquake scenario. Cases in which minimising downtime is prioritised (e.g., Case 6) result in an optimal decision of $\bar{A}$ for most values of examined $E[Sd_{geom}|M^*, R^*]$, whereas cases in which minimising casualties are heavily prioritised (e.g., Case 2) tend to result in an optimal decision of A, particularly for higher values of examined $E[Sd_{geom}|M^*, R^*]$. Note that there is no sharp transition between an optimal decision of $\bar{A}$ and A in terms of $E[Sd_{geom}|M^*, R^*]$, since A_{opt} also depends on t_{EEW} (and thus n) and possibly $\boldsymbol{d}$. It is also observed that $A_{opt}(\boldsymbol{d}, t_{EEW})$ approaches $A_{opt}(M^*, t_{EEW})$ for $n = 34$. The cases shown demonstrate the inherent EEW trade-off between efficient decisions that maximise the risk-mitigation

opportunity of A and more accurate decisions that require waiting for further information from a larger number of triggered stations.

3.7 Assessing the Effectiveness of the Developed EEW-DSS System

Tables 3 to 6 present values of $E[VoI_{1,j}(\boldsymbol{d}, t_{EEW})]$and $E[VoI_{2,j}(\boldsymbol{d}, t_{EEW})]$ associated with various n, which can be used to further investigate EEW benefits for variations in the trade-off between accuracy and timeliness, across different sets of w_j (detailed in Table 2). $E[VoI_{1,1}(\boldsymbol{d}, t_{EEW})]$ values in Table 3 display convergence towards zero for downtime-dominated weighting cases, but are negative for casualty-dominated cases in which $A_{opt}(\boldsymbol{d}, t_{EEW})$=$A$ creates unnecessary inspection downtimes. $E[VoI_{1,2}(\boldsymbol{d}, t_{EEW})]$ values presented in Table 4 are positive for casualty-dominated weighting strategies and gradually become zero for w_j cases that place increasing priority on minimising downtime (towards Case #7), as $A_{opt}(\boldsymbol{d}, t_{EEW})$ tends to transition from A to $\bar{A}$ (see Figure 14).

$E[VoI_{2,1}(\boldsymbol{d}, t_{EEW})]$ and $E[VoI_{2,2}(\boldsymbol{d}, t_{EEW})]$ values are presented in Tables 5 and 6, respectively, where it may be observed that an EEW based on perfect source-parameter estimates provides no (or little) value: (1) if n is relatively high, when losses associated with $\boldsymbol{d}$ become close to those of M^*; and/or (2) if a stakeholder is only interested in minimising casualties (Case #1) because $A_{opt}(M^*, t_{EEW}) = A_{opt}(\boldsymbol{d}) = A$ for all n and earthquake scenarios considered (see Figure 14). Positive values of (1) $E[VoI_{2,2}(\boldsymbol{d}, t_{EEW})]$ (for larger weighting cases and smaller n values) and (2) $E[VoI_{2,1}(\boldsymbol{d}, t_{EEW})]$ values (for Case #2 in particular) respectively underline the benefits of avoiding missed and false alarms with perfect information.

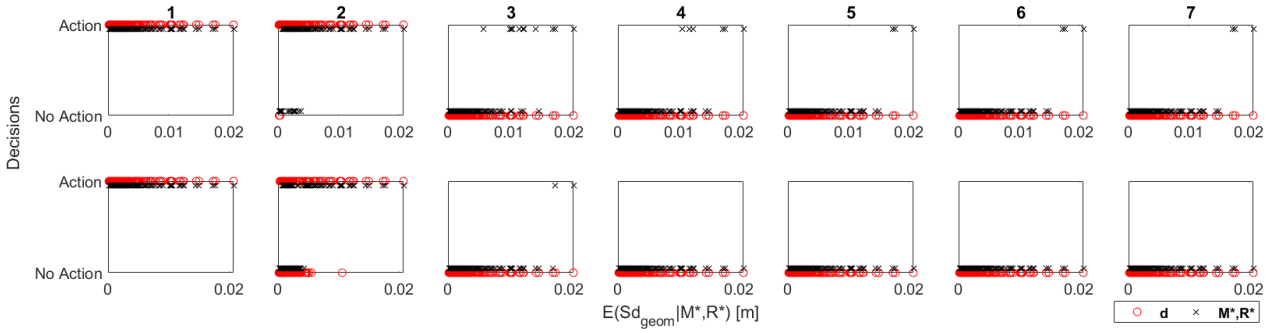

Figure 14. Optimal decisions for different w_j cases (numbered in bold). The top row displays decisions for n=1 (and the associated lead time), and the bottom row provides these for the lead time and information associated with n=34.

Table 3. $E[VoI_{1,1}(\boldsymbol{d}, t_{EEW})] \cdot 10^3$ for various n used to compute $\boldsymbol{d}$

		n					
		1	2	4	8	16	32
w_j Case no	1	-2.2173	-2.3060	-2.4375	-2.6327	-2.9696	-3.3028
	2	-2.2106	-2.2199	-2.0893	-1.7451	-0.8987	-0.2652
	3	0.0000	0.0011	-0.0001	-0.0048	-0.0033	0.0000
	4	0.0000	0.0000	0.0000	-0.0014	-0.0001	0.0000
	5	0.0000	0.0000	0.0000	0.0000	0.0000	0.0000
	6	0.0000	0.0000	0.0000	0.0000	0.0000	0.0000
	7	0.0000	0.0000	0.0000	0.0000	0.0000	0.0000

Table 4. $E[VoI_{1,2}(\boldsymbol{d}, t_{EEW})] \cdot 10^3$ for various n used to compute $\boldsymbol{d}$

	n

		1	2	4	8	16	32
w_j Case no	1	0.4734	0.4344	0.3823	0.3201	0.2338	0.1624
	2	0.4734	0.4303	0.3819	0.3140	0.2275	0.1495
	3	0.0000	0.0636	0.0694	0.0911	0.0810	0.0000
	4	0.0000	0.0000	0.0000	0.0090	0.0326	0.0000
	5	0.0000	0.0000	0.0000	0.0000	0.0000	0.0000
	6	0.0000	0.0000	0.0000	0.0000	0.0000	0.0000
	7	0.0000	0.0000	0.0000	0.0000	0.0000	0.0000

Table 5. $E\left[VoI_{2,1}(\boldsymbol{d}, t_{EEW})\right] \cdot 10^3$ for various n used to compute $\boldsymbol{d}$

		n					
		1	2	4	8	16	32
w_j Case no	1	0.0000	0.0000	0.0000	0.0000	0.0000	0.0000
	2	1.2002	1.1875	1.0483	0.7962	0.3150	-0.0042
	3	-0.0043	-0.0044	-0.0035	0.0028	0.0022	-0.0015
	4	0.0005	0.0012	0.0010	0.0017	-0.0002	0.0000
	5	0.0022	0.0019	0.0010	0.0002	-0.0003	0.0000
	6	0.0022	0.0019	0.0010	0.0005	0.0000	0.0000
	7	0.0022	0.0019	0.0011	0.0005	0.0000	0.0000

Table 6. $E\left[VoI_{2,2}(\boldsymbol{d}, t_{EEW})\right] \cdot 10^3$ for various n used to compute $\boldsymbol{d}$

		n					
		1	2	4	8	16	32
w_j Case no	1	0.0000	0.0000	0.0000	0.0000	0.0000	0.0000
	2	-0.0006	0.0035	-0.0005	0.0048	0.0035	0.0077
	3	0.3034	0.1889	0.1427	0.0477	-0.0011	0.0357
	4	0.2285	0.1725	0.1292	0.0999	0.0306	0.0000
	5	0.1631	0.1524	0.1292	0.1090	0.0632	0.0000
	6	0.1631	0.1524	0.1292	0.0823	0.0000	0.0000
	7	0.1631	0.1524	0.0963	0.0823	0.0000	0.0000

4. Conclusions

This paper introduced a novel EEW-DSS that is specifically designed for mitigating seismic risk at a railroad bridge. An enhanced engineering-oriented approach was used to create this system, which also integrates multi-criteria decision making (MCDM) theory to account for varying stakeholder priorities towards different types of seismic risk. The benefits of the proposed EEW-DSS were uniquely quantified in terms of bespoke VoI metrics that accounted for the risk preferences input to the MCDM component, as well as the range of possible earthquake scenarios that may affect the bridge. Below is a list of the most important outcomes from this study:

- It is found that optimal EEW decisions or actions strongly depend on which consequence is prioritised based on stakeholder interests. This is consistent with the conclusions of previous studies that have incorporated MCDM in EEW decision making. For example, prioritising the minimisation of casualties can result in issuing EEW alarms even at small levels of shaking (since false alarms do not cause related losses), which is not the case when priority is placed on minimising downtime. Optimal decisions are also influenced by the accuracy of EEW estimations (increasing with the number of stations triggered) as well as the lead time available for risk-reduction efforts (decreasing with the number of stations triggered).
- Thus, the number of triggered stations used in the EEW-DSS (and the decreasing lead time available to facilitate EEW) has competing effects on its effectiveness. Increasingly accurate source-parameter predictions yielded by larger amounts of recording station data result in more accurate optimal decisions but also decrease the effectiveness of EEW due to the amplified risks of train derailment as lead time shortens.
- Findings of the case study indicate that there is often no (or even negative) gain in risk mitigation achieved from an EEW-DSS system, particularly for minimising downtime. This is due to the fact that no action (i.e., not slowing down trains) is often the optimal decision for the low ground-shaking values that dominate the

seismic hazard of the case-study area, for which issuing an EEW alarm would only unnecessarily trigger a disruptive bridge inspection.

- The benefits of having perfect source-parameter information in the EEW-DSS can depend on the loss priorities of stakeholders. Findings of the case study imply that stakeholders who only care about minimising casualties would experience little to no marginal benefits in having a perfect EEW-DSS, since the more uncertain loss estimates obtained with the raw EEW parameters still lead to the correct optimal decision (i.e., trigger the alarm). On the other hand, stakeholders that heavily prioritise the minimisation of downtime losses do benefit from the use of perfect information, since it can eliminate some missed alarm opportunities associated with the more uncertain source-parameter estimates.
- The benefits of having perfect source-parameter information in the EEW-DSS also depends (as expected) on the number of triggered stations used in the EEW-DSS. Larger numbers of triggered stations result in more reliable source-parameter estimates that then diminish the value of a perfect system.

It is important to acknowledge that while the results of the case-study application provide some useful insights on the benefits of adopted risk-informed EEW decision making for railway bridges, they have not been validated in a real-life setting and should only be considered demonstrative. Furthermore, seismic hazard is low for the specific testbed examined and findings could change for regions with higher seismic hazard. This study considered one possible EEW risk-mitigation action, whereas a more realistic EEW strategy could involve multiple possible actions that slow the train to different speeds or even activate structural control systems for the case-study bridge. More advanced derailment mechanisms can be simulated through vehicle-bridge interaction techniques, which have received attention in the last two decades, some of which centre on earthquake-induced derailment.

This study considered only one node (i.e., a bridge) in a railway system; a more advanced methodology would be required to measure the benefits of EEW on a holistic system-level scale that captures all nodes in the network. This methodology would involve: (1) computing consequences for multiple bridges; (2) accounting for the cascading implications of node-level actions, such as the knock-on disruptions caused by a bridge closure across the entire network; and (3) developing an approach for unifying the complete set of consequences in MCDM. (1) and (3) would require an advanced network-level analysis technique, such as agent-based modelling (Feng et al., 2020), For (2), the MCDM process might involve the use of spatially-dependent weightings for the different loss metrics (i.e., criteria), if necessary. Spatial discrepancies in weightings may reflect diverse socioeconomic or political backgrounds of stakeholders in different regions, for instance. However, the network-level version of the EEW-DSS could also account for consequences in a more aggregated manner (e.g., total disruption in railway traffic flow). Furthermore, the EEW-DSS could take advantage of any structural health monitoring infrastructure installed on transportation network. This type of infrastructure, which would consist of additional accelerometers, could help to better constrain the estimated characteristics of an incoming event as well as the seismic demand to be experienced by the bridge.

Funding Details

This paper is supported by the European Union's Horizon 2020 research and innovation programme under grant agreement No 821046, project TURNkey (Towards more Earthquake-resilient Urban Societies through a Multi-sensor-based Information System enabling Earthquake Forecasting, Early Warning and Rapid Response actions).

Disclosure statement

The authors report there are no competing interests to declare.

References

Akkar, S., Sandıkkaya, M. A., & Bommer, J. J. (2014). Empirical ground-motion models for point-and extended-source crustal earthquake scenarios in Europe and the Middle East. *Bulletin of Earthquake Engineering*, *12*(1), 359-387.

Allen, R. M., & Kanamori, H. (2003). The potential for earthquake early warning in southern California. *Science*, *300*(5620), 786-789.

Attarchian, N., Kalantari, A., & Moghadam, A. S. (2018). Developing a new procedure for evaluating the ductility capacity of rectangular RC piers subjected to biaxial flexural loadings. *Engineering Structures, 172,* 187-200.

Banerjee, S., & Shinozuka, M. (2008). Mechanistic quantification of RC bridge damage states under earthquake through fragility analysis. *Probabilistic Engineering Mechanics, 23*(1), 12-22.

Bazzurro, P., Cornell, C. A., Shome, N., & Carballo, J. E. (1998). Three proposals for characterising MDOF nonlinear seismic response. *Journal of Structural Engineering, 124*(11), 1281-1289.

Cheng, M. H., Wu, S., Heaton, T. H., & Beck, J. L. (2014). Earthquake early warning application to buildings. *Engineering Structures*, *60*, 155-164.

Colombelli, S., Caruso, A., Zollo, A., Festa, G., & Kanamori, H. (2015). AP wave-based, on-site method for earthquake early warning. *Geophysical Research Letters*, *42*(5), 1390-1398.

Cornell, C. A. (1964). *Stochastic processes in civil engineering*. [Doctoral dissertation, Stanford University].

Cremen, G., Bozzoni, F., Pistorio, S., & Galasso, C. (2022). Developing a risk-informed decision-support system for earthquake early warning at a critical seaport. *Reliability Engineering & System Safety, 218*, 108035.

Cremen, G., & Galasso, C. (2020). Earthquake early warning: Recent advances and perspectives. *Earth-Science Reviews, 205*, 103184.

Cremen, G., & Galasso, C. (2021). A decision-making methodology for risk-informed earthquake early warning. *Computer-Aided Civil and Infrastructure Engineering, 36*(6), 747-761.

Cremen, G., Velazquez, O., Orihuela, B., & Galasso, C. (2021). Predicting approximate seismic responses in multistory buildings from real-time earthquake source information, for earthquake early warning applications. *Bulletin of Earthquake Engineering, 19*(12), 4865-4885.

Cremen, G., Zuccolo, E., & Galasso, C. (2021). Accuracy and uncertainty analysis of selected methodological approaches to earthquake early warning in Europe. *Seismological Research Letters 92*(4), 2321-2332.

Ebrahimi, H., Sattari, F., Lefsrud, L., & Macciotta, R. (2021). Analysis of train derailments and collisions to identify leading causes of loss incidents in rail transport of dangerous goods in Canada. *Journal of Loss Prevention in the Process Industries, 72*, 104517.

Feng, K., Li, Q., & Ellingwood, B. R. (2020). Post-earthquake modelling of transportation networks using an agent-based model. *Structure and Infrastructure Engineering*, 16(11), 1578-1592.

Galasso, C., Zuccolo, E., Aljawhari, K., Cremen, G., & Melis, N. S. (2023). Assessing the potential implementation of earthquake early warning for schools in the Patras region, Greece. *International Journal of Disaster Risk Reduction, 90*, 103610.

Giardini, D., et al. (2013). Seismic Hazard Harmonisation in Europe (SHARE): Online Data Resource, http://portal.share-eu.org:8080/jetspeed/portal/, doi: 10.12686/SED-00000001-SHARE.

Guillaud, L. M. (2006). *Probability of derailment under earthquake conditions* [Master's thesis, Massachusetts Institute of Technology].

Heaton, T. H. (1985). A model for a seismic computerised alert network. *Science*, *228*(4702), 987-990.

Hilbring, D., Titzschkau, T., Buchmann, A., Bonn, G., Wenzel, F., & Hohnecker, E. (2014). Earthquake early warning for transport lines. *Natural Hazards*, *70*(3), 1795-1825.

Howard, R. A. (1966). Information value theory. *IEEE Transactions on Systems Science and Cybernetics, 2*(1), 22-26.

Iervolino, I., Convertito, V., Giorgio, M., Manfredi, G., & Zollo, A. (2006). Real-time risk analysis for hybrid earthquake early warning systems. *Journal of Earthquake Engineering*, *10*(6), 867-885.

Iervolino, I., Giorgio, M., Galasso, C., & Manfredi, G. (2009). Uncertainty in early warning predictions of engineering ground motion parameters: What really matters?. *Geophysical Research Letters*, *36*(5) L00B06.

Iervolino, I., Giorgio, M., & Manfredi, G. (2007). Expected loss-based alarm threshold set for earthquake early warning systems. *Earthquake Engineering & Structural Dynamics*, *36*(9), 1151-1168.

Karim, K. R., & Yamazaki, F. (2001). Effect of earthquake ground motions on fragility curves of highway bridge piers based on numerical simulation. *Earthquake Engineering & Structural Dynamics, 30*(12), 1839-1856.

Laske, G., Masters, G., Ma, Z., & Pasyanos, M. (2013, April 7-12). Update on CRUST1. 0—A 1-degree global model of Earth's crust. *Geophysical Research Abstracts (15) 2658*. EGU General Assembly, Vienna, Austria.

Le Guenan, T., Smai, F., Loschetter, A., Auclair, S., Monfort, D., Taillefer, N., & Douglas, J. (2016). Accounting for end-user preferences in earthquake early warning systems. *Bulletin of Earthquake Engineering*, *14*(1), 297-319.

Manterola Armisén, J., Martinez Cutillas, A., Navarro, J. A., & Fuente Garcia, S. (2008, November 24-27). *Puentes de ferrocarril de alta velocidad en el tramo internacional Figueras-Perpignan*. IV Congreso de la Asociacion Cient-tecnica del Hormiguon Estructural - Congreso Internacional de Estructuras. Valencia, Spain.

Martínez-Martín, F. J., González-Vidosa, F., Hospitaler, A., & Yepes, V. (2013). A parametric study of optimum tall piers for railway bridge viaducts. *Structural Engineering and Mechanics, 45*(6), 723-740.

McKenna, F. (2011). OpenSees: a framework for earthquake engineering simulation. *Computing in Science & Engineering, 13(*4), 58-66.

Minson, S. E., Baltay, A. S., Cochran, E. S., Hanks, T. C., Page, M. T., McBride, S. K., Milner, K. R., & Meier, M. A. (2019). The limits of earthquake early warning accuracy and best alerting strategy. *Scientific Reports*, *9*(1), 1-13.

Minson, S. E., Meier, M. A., Baltay, A. S., Hanks, T. C., & Cochran, E. S. (2018). The limits of earthquake early warning: Timeliness of ground motion estimates. *Science Advances*, *4*(3), eaaq0504.

Minson, S. E., Wu, S., Beck, J. L., & Heaton, T. H. (2017). Combining multiple earthquake models in real time for earthquake early warning. *Bulletin of the Seismological Society of America*, *107*(4), 1868-1882.

Muga Viaduct. Retrieved February 17, 2021, from https://structurae.net/fr/ouvrages/viaduc-de-la-muga

Muntasir Billah, A. H. M., & Shahria Alam, M. (2015). Seismic fragility assessment of highway bridges: a state-of-the-art review. *Structure and Infrastructure Engineering, 11*(6), 804-832.

Nakamura, Y. (2005). Earthquake early warning and derailment of Shinkansen train at the 2004 Niigataken-Chuetsu earthquake. *Environmental Systems Research*, *28*, 115-115.

Nakamura, Y., Saita, J., & Sato, T. (2011). On an earthquake early warning system (EEW) and its applications. *Soil Dynamics and Earthquake Engineering*, *31*(2), 127-136.

Ozer, E., Cremen, G., Galasso, C., Gehl, P., & Tubaldi, E. (2023, July 9-13). An Earthquake Early Warning Decision Support System for Railway Bridge Infrastructure. *14th International Conference on Application of Statistics and Probability in Civil Engineering*. Trinity College Dublin, Dublin, Ireland.

Pitilakis, K., Karapetrou, S., Bindi, D., Manakou, M., Petrovic, B., Roumelioti, Z., Boxberger, T., & Parolai, S. (2016). Structural monitoring and earthquake early warning systems for the AHEPA hospital in Thessaloniki. *Bulletin of Earthquake Engineering*, *14*(9), 2543-2563.

Pozzi, M., & Der Kiureghian, A. (2011, April 18). Assessing the value of information for long-term structural health monitoring. *Health monitoring of structural and biological systems, (7984), 79842W*. International Society for Optics and Photonics. San Diego, {California} United States.

RENFE NSCF. Retrieved January 1, 2021, from https://www.renfe-sncf.com/rw-en/Pages/Home.aspx

Shimamura, M., & Yamamura, K. (2006). Development of Shinkansen Earthquake Impact Assessment System. *JR East Technical Review*, (7), 56-64.

Sokos, E., Tselentis, G. A., Paraskevopoulos, P., Serpetsidaki, A., Stathopoulos-Vlamis, A., & Panagis, A. (2016). Towards earthquake early warning for the Rion-Antirion bridge, Greece. *Bulletin of Earthquake Engineering*, *14*(9), 2531-2542.

Strauss, J. A., & Allen, R. M. (2016). Benefits and costs of earthquake early warning. *Seismological Research Letters, 87*(3), 765-772.

Thöns, S., & Faber, M. H. (2013, June 16-20). Assessing the value of structural health monitoring. *11th International conference on structural safety and reliability-Safety, reliability, risk and lifecycle performance of structures and infrastructures* (pp. 1-8). CRC Press, New York, United States.

TGV Duplex. Retrieved February 7, 2023, from https://en.wikipedia.org/wiki/TGV_Duplex

Tubaldi, E., Ozer, E., Douglas, J., & Gehl, P. (2021). Examining the contribution of near real-time data for rapid seismic loss assessment of structures. *Structural Health Monitoring 21*(1), 118-137.

Wald, D. J., & Allen, T. I. (2007). Topographic slope as a proxy for seismic site conditions and amplification. *Bulletin of the Seismological Society of America*, *97*(5), 1379-1395.

Wald, D. J. (2020). Practical limitations of earthquake early warning. *Earthquake Spectra*, *36*(3), 1412-1447.

Woessner, J., Danciu, L., Giardini, D., Crowley, H., Cotton, F., Grünthal, G., et al. (2015). The 2013 European seismic hazard model: key components and results. *Bulletin of Earthquake Engineering, 13*(12), 3553–3596.

Wu, Y. M., & Kanamori, H. (2008). Development of an earthquake early warning system using real-time strong motion signals. *Sensors*, *8*(1), 1-9.

Wu, S., Beck, J. L., & Heaton, T. H. (2013). ePAD: Earthquake probability-based automated decision-making framework for earthquake early warning. *Computer-Aided Civil and Infrastructure Engineering*, *28*(10), 737-752.

Yoon, K. P., & Hwang, C. L. (1995). *Multiple attribute decision making: an introduction*. Sage publications.

Zhang, W. H., Lu, D. G., Qin, J., Thöns, S., & Faber, M. H. (2021). Value of information analysis in civil and infrastructure engineering: a review. *Journal of Infrastructure Preservation and Resilience, 2*(1), 1-21.

Zonta, D., Glisic, B., & Adriaenssens, S. (2014). Value of information: impact of monitoring on decision-making. *Structural Control and Health Monitoring, 21*(7), 1043-1056.

Zuccolo, E., Cremen, G., & Galasso, C. (2021). Comparing the performance of regional earthquake early warning algorithms in Europe. *Frontiers in Earth Science*, *9*, 425.